
Seeds Cleansing CNMF for Spatiotemporal Neural Signals Extraction of Miniscope Imaging Data

Jinghao Lu¹, Chunyuan Li³, Fan Wang^{1,2}

¹Department of Neurobiology and

²Cell Biology, Duke University Medical Center, and

³Electrical and Computer Engineering

Duke University, Durham, NC 27708

{jinghao.lu, cl319, fan.wang}@duke.edu

Abstract

Miniscope calcium imaging is increasingly being used to monitor large populations of neuronal activities in freely behaving animals. However, due to the high background and low signal-to-noise ratio of the single-photon based imaging used in this technique, extraction of neural signals from the large numbers of imaged cells automatically has remained challenging. Here we describe a highly accurate framework for automatically identifying activated neurons and extracting calcium signals from the miniscope imaging data, seeds cleansing Constrained Nonnegative Matrix Factorization (sc-CNMF). This sc-CNMF extends the conventional CNMF with two new modules: *i*) a *neural enhancing* module to overcome miniscope-specific limitations, and *ii*) a *seeds cleansing* module combining LSTM to rigorously select and cleanse the set of seeds for detecting regions-of-interest. Our sc-CNMF yields highly stable and superior performance in analyzing miniscope calcium imaging data compared to existing methods.

1 Introduction

In neuroscience, calcium imaging has become one of the staple technologies to simultaneously monitor the activities from a large population of neurons in awake and behaving animals [1–4]. In most experiments, the target neurons express genetically encoded calcium indicators, and transiently change their fluorescence levels reflecting dynamic calcium concentrations within the neurons.

Two-photon microscopy is the most commonly used method for *in vivo* calcium imaging, which produces high quality videos over the imaging plane with relatively low and stable background [1, 2]. A rich line of work has leveraged this advantage to extract calcium signals, including the popular PCA/ICA method [5, 6], K-SVD dictionary learning [7], Nonnegative Matrix Factorization [8], Constrained Nonnegative Matrix Factorization (CNMF) [9] and sliding window convolutional network [10]. However, animals are head-restrained and unable to move freely under the two-photon setup. Furthermore, imaging deep brain regions in awake behaving animals using two-photon microscopy remains challenging.

Recently, advances in integrated *miniscope technology* enables imaging of large neural populations possible in freely behaving animals [3, 4, 11]. This technology allows neuroscientists to study cortical and subcortical neural circuits using a rich repertoire of animal behaviors. However, there are two major challenges in adopting the miniscope imaging for neural activities with cellular resolutions recording. First, the miniscope imaging is a single-photon-based technology that results in much noisier data, and innegligibly uneven and unstable background fluctuations, compared to two-photon microscopy [12]. These challenges result in the failure of directly applying previous two-photon imaging algorithms in properly extracting calcium signals from the miniscope imaging data. Second,

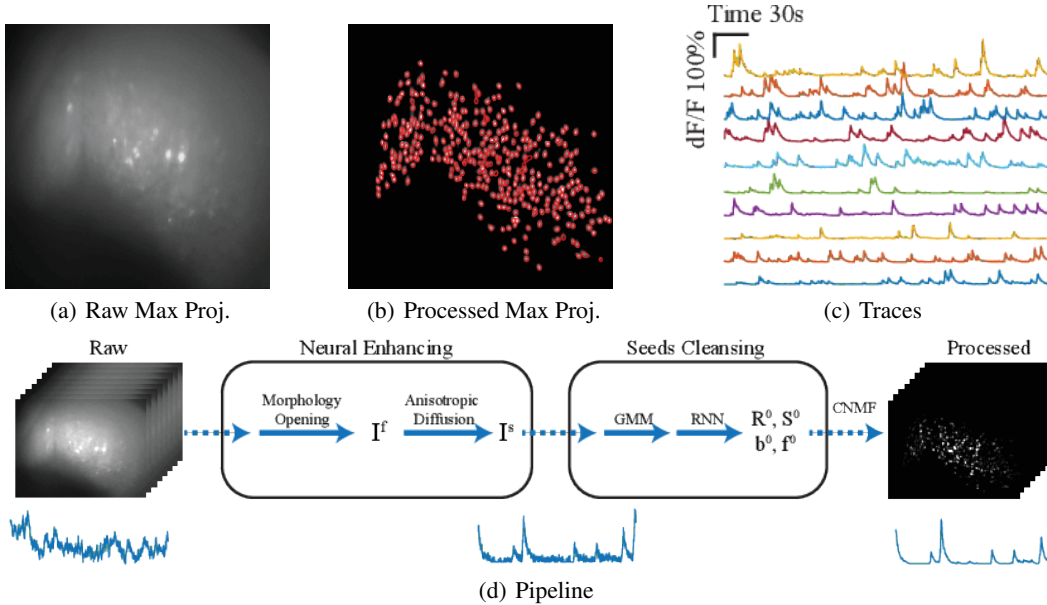


Figure 1: Problem illustration: neural signals extraction from miniscope imaging. (a) Max projection of raw video. (b) Max projection of fully processed video with identified ROIs in the contours. (c) Extracted neural signals. (d) Pipeline of the proposed methods.

neural activities during hundreds of behavioral sessions are often recorded, with each session easily containing GB size of data. Therefore, manual annotation becomes increasingly laborious and even impossible in cases of large-scale datasets as well as unreliable (*i.e.* failure in detecting overlapping and low-activity neurons).

To overcome these challenges, we develop the seeds cleansing Constrained Nonnegative Matrix Factorization (sc-CNMF) to extract calcium activity signals from the in vivo miniscope imaging videos. Our sc-CNMF can accurately locate the regions of interest (ROIs), and yield the calcium signal of the corresponding neurons (see Fig. 1(a-c)). Specifically, we extend the pure CNMF in two fronts, with the following contributions *i)* A general *neural enhancing* module is designed for the single-photon calcium imaging data that minimizes the influence of background instability and fluctuation. *ii)* More importantly, the *seeds cleansing* module is proposed to reliably detect the population of ROIs, and thus significantly boost the performance in processing miniscope imaging data by maximizing both the precision and recall with increased efficiency. We emphasize that our seeds cleansing is non-trivial. It consists of two steps: a Gaussian Mixture Model (GMM) followed by a Long Short-Term Memory (LSTM) based processing to identify seeds for ROIs [13]. A typical pipeline of our algorithm is shown in Fig. 1(d).

Related Work Previous algorithms for automatic extraction of calcium signals from imaging videos can be divided into three categories: linear unsupervised basis learning methods [5–7], nonlinear unsupervised basis learning methods [8, 9], and the supervised learning method [10]. The first and most popular algorithm, PCA/ICA, applies PCA as a simple preprocessing step for dimension reduction and noise removal [14], and then applies spatiotemporal-ICA to segment individual ROIs and their time series. Though proposed to be fast and efficient, algorithms such as PCA/ICA are endogenously based on the assumption of linearity, thus failing in separating spatially overlapping ROIs or returning localized ROIs. Later works integrated more subtle considerations of

	sc-CNMF	PCA/ICA	CNMF
Neural Enhancing	✓	Minor	–
Seeds Cleansing	✓	–	Moderate
Spatial Localization	✓	–	✓
Temporal Deconvolution	✓	–	✓
Overlapping Separation	✓	–	✓
Automatic Merging	✓	–	Moderate
Parameter Tuning	Minimal	✓	✓

Table 1: Methods Comparison. “✓” indicates features integrated in the methods, while “–” indicates not.

nonlinearity [8, 9]. CNMF further combines nonlinearity in matrix factorization with simultaneous deconvolving spike trains from calcium dynamics [9], which returns more spatially localized maps of ROIs compared to the previous methods. A recent work, sliding window convolutional networks [10], is the first attempt to use supervised deep learning to tackle the problem. However, these previous methods all depend on either sophisticated parameter tuning or only applicable for two-photon imaging. In this work, we choose PCA/ICA and CNMF as our comparing references, and we summarize the features of the different algorithms in Table 1.

2 Preliminaries on CNMF

The pure CNMF in our method is used to deconvolve neural populations and demix their calcium dynamics. Specifically, for the video data $\mathbf{X} \in \mathbb{R}^{P \times T}$ (P is number of pixels per frame, and T is number of frames), the CNMF decomposes \mathbf{X} into a spatial dictionary $\mathbf{R} \in \mathbb{R}^{P \times K}$, potentially individual ROIs (where K is the number of identified ROIs), and corresponding temporal dynamics matrix $\mathbf{S} \in \mathbb{R}^{T \times K}$, in addition to the background \mathbf{B} and the noise \mathbf{E} : $\mathbf{X} = \mathbf{R}\mathbf{S}^\top + \mathbf{B} + \mathbf{E}$. Similarly, with the rank-1 assumption on \mathbf{B} , CNMF decomposes the background $\mathbf{B} = \mathbf{b}\mathbf{f}^\top$, where $\mathbf{b} \in \mathbb{R}^P$ and $\mathbf{f} \in \mathbb{R}^T$. Meanwhile, \mathbf{S} is also correlated with underlying action potential events: $\mathbf{A} = \mathbf{S}^\top \mathbf{G}$, where $\mathbf{A} \in \mathbb{R}^{K \times T}$, and $\mathbf{G} \in \mathbb{R}^{T \times T}$ is the second-order autoregressive matrix. The parameters $\mathbf{R}, \mathbf{S}, \mathbf{b}, \mathbf{f}$ in CNMF are estimated via iteratively alternating between the following two steps [9].

Estimating Spatial Parameters Given the estimates of temporal parameters $\mathbf{S}^{(\ell-1)}$ and $\mathbf{f}^{(\ell-1)}$ from the last iteration, the spatial parameters can be updated by solving the problem: $\min_{\mathbf{R}, \mathbf{b}} \|\mathbf{R}\|_1$, subject to $\mathbf{R}, \mathbf{b} \geq 0$ and $\|\mathbf{X}(i, :) - \mathbf{R}(i, :)\mathbf{S}^{(\ell-1)\top} - \mathbf{b}(i)\mathbf{f}^{(\ell-1)\top}\| \leq \epsilon_i \sqrt{T}$, where $\mathbf{X}(i, :)$ is the i th row of the matrix \mathbf{X} , $\mathbf{b}(i, :)$ is the i th element of the vector. $\epsilon_i \sqrt{T}$ is the empirically selected noise residual constraint of the corresponding pixel. This is essentially a basis pursuit denoising problem, and it is solved by the least angular regression [15] in implementation.

Estimating Temporal Parameters Given the estimates of spatial parameters \mathbf{R}, \mathbf{b} and temporal parameters $\mathbf{S}^{(\ell-1)}, \mathbf{f}^{(\ell-1)}$ from the last iteration, the temporal parameters can be updated by solving the problem: $\min_{\mathbf{S}, \mathbf{f}} \sum_{k=1}^K \mathbf{1}^\top \mathbf{G} \mathbf{S}$, subject to $\mathbf{G} \mathbf{s}_k \geq 0, k = 1 \cdots K$ and $\|\mathbf{X}(i, :) - \mathbf{R}(i, :)\mathbf{S}^{(\ell-1)} - \mathbf{b}(i)\mathbf{f}^{(\ell-1)\top}\| \leq \epsilon_i \sqrt{T}$.

3 sc-CNMF

The performance of pure CNMF is limited in the following three aspects: *i*) It requires the product of an ROI guess and corresponding dynamics subtracted from the residual each iteration to initialize the rest ROI seeds. Therefore, the spatial maps of the remaining ROIs are dependent on the previous iterations, which renders CNMF very sensitive to the initial guesses of the ROI location. *ii*) The number of ROIs K is unknown in practice but the algorithm requires it manually set by users. CNMF will yield a higher true negative ratio if K is too low, or many false positives if K is set too high. While it is possible to manually decrease false positives, the missed ROIs can never be rescued back. *iii*) The iterative initialization nature of CNMF requires sequential execution of the algorithm.

To overcome the above limitations, we developed two modules, the neural enhancing and seeds cleansing, to provide good initialization for downstream modified pure CNMF in this section.

3.1 Neural Enhancing

Existing works either employ naïve video cleaning operations (PCA/ICA) or assume low-rank background dynamics (rank-1 in CNMF). However, in single-photon miniscope imaging, the background cannot be well approximated by rank-1 decomposition due to the non-uniform illumination and large temporal fluctuation of the background. Here we propose a two-step neural enhancing module.

Background Removal We propose to separate the foreground neural signals from the background in a frame-wise fashion. We denote $\mathbf{I} \in \mathbb{R}^{M \times J}$ as a single frame of the video \mathbf{X} before vectorization, *i.e.* $\text{vec}(\mathbf{I}) = \mathbf{X}(:, t), t \in \{1, \dots, T\}$, where M, J are the width and height of the image. Based on the observation that neuronal ROIs are small in size compared to background structures, the

gray-scale morphological opening operator with a flat *structuring element matrix* Φ can well separate the background \mathbf{B} from the image \mathbf{I} adaptively. In particular, the opening operator is the combination of erosion \ominus and dilation \oplus : $\mathbf{B} = (\mathbf{I} \ominus \Phi) \oplus \Phi$ [16], where the morphological erosion returns minimum value and dilation returns maximum value within the same structuring window at each point. In practice, the size of Φ is set comparable to the size of ROIs in the imaging field. The foreground is then computed as: $\mathbf{I}^f = \mathbf{I} - \mathbf{B}$. After the dynamic background removal, \mathbf{I}^f contains only neuronal information with minimal background corruption.

Denoising Though the influence of fluctuating background is maximally suppressed, the sparse yet sharp spatial noise randomly embedded within each frame remains possible to contaminate the neural information. To remove the spatial noise within ROIs and in the background, we apply denoising operation on \mathbf{I}^f using anisotropic diffusion [17]. For a given diffusion time τ , the evolution follows the equation $\frac{\partial \mathbf{I}^f}{\partial \tau} = \text{div}(\mathbf{C}\nabla \mathbf{I}^f) \triangleq \nabla \mathbf{C} \cdot \nabla \mathbf{I}^f + \mathbf{C}\Delta \mathbf{I}^f$ where \mathbf{C} is the diffusive coefficient matrix depending on pixels and τ . By choosing concrete form of \mathbf{C} and τ , we can control the smoothing level along or perpendicular to the boundaries between neurons and the background. Due to the simple structures in the cleaned imaging field, we choose the classical Perona-Malik filter $\mathbf{C} = \exp\left(-\frac{\|\nabla \mathbf{I}^f\|^2}{\kappa^2}\right)$, where κ controls the threshold of high-contrast. The diffusivity is selected to preferentially smooth high-contrast regions, and κ and τ are chosen to allow high tolerance. The output image \mathbf{I}^s contains reduced spatial noise while preserves the boundary information of ROIs.

3.2 Seeds Cleansing

Previous work either contains no explicit initialization step to obtain the complete ROI set reliably (e.g. PCA/ICA), or initializes by solving a convex optimization problem (CNMF). However, these initializations usually fail in the case of highly dominant and dynamic background, where the approximation does not hold. Moreover, a problem of previous initialization methods is that the subsequently initialized components are dependent on the preceding results, and the quality of the initialization significantly relies on the users' inputs of parameters. We believe that, therefore, an accurate initialization process is necessary for achieving convergence to the correct ROI set as well as for reducing information loss/duplication. In this section, we generate and cleanse the potential seeds of ROIs, and create the initial spatial regions and the time series of these ROIs for the final refinement of spatiotemporal signals.

Over-complete Seeds Initialization In order to generate the initial set containing centers of all potential ROIs, we construct a *randomized max pooling* process to create an over-complete set of seeds. This process first randomly selects a portion of frames $\mathbf{I}_\alpha^s = \{\mathbf{I}_t^s\}_{t \in \alpha}$, $\alpha \subseteq \{1, \dots, T\}$, where α is a randomized subset of frame number. We then compute the max-projection map across selected frames $\mathbf{I}^{\max} = \max(\mathbf{I}_\alpha^s)$, and further detect all the local max points on this map as \mathcal{S} . We repeat the above procedures multiple times, and collect the union of each map \mathcal{S} as the final over-complete set of neural seeds $\mathcal{S}_{\text{seeds}}$. Our randomized max pooling can improve the true positive rate compared with max-pooling over the entire video, because a true seed can be buried in the uneven florescence of an ROI over a long period but can most likely be discovered in a small temporal vicinity. To exclude false positive seeds from the set, we propose the following two-stage algorithm for seeds refinement.

Seeds Refinement with GMM The temporal properties of ROI and non-ROI can be very different. ROIs often have prominent peak-valley difference d , while non-ROIs tend to be less spiky. We assume $\{d_s | s \in \mathcal{S}_{\text{seeds}}\}$ are generated from a mixture of two Gaussians $d_s \sim \sum_{i=1}^2 \omega_i \mathcal{N}(d | \mu_i, \sigma_i^2)$ where $\mu_i, \sigma_i^2, \omega_i$ indicate the mean, variance, mixture proportion of the i th Gaussian component. Therefore, we can cluster the seeds based on their probabilities of belonging to each component, and only consider those having higher probabilities to the Gaussian with a larger mean as positive seeds.

Seeds Refinement with LSTM To select true ROI seeds from the over-complete set, we need to characterize the patterns of neuronal calcium dynamics. Previous methods include using biophysical frameworks with minimal priors [18], and low-order autoregressive process [19], with the assumption that there exists clear stereotypical calcium spike patterns. However, in the miniscope imaging data intrinsically corrupted with large noise, the sequences (the neuronal calcium trace) can be complex. Hence we propose to employ Recurrent Neural Networks (RNNs) [20] for calcium signal sequence modeling and classification.

We offline train the RNNs with a separate training dataset, composed of both positive and negative sequence chunks of length $T_0 = 100$, obtained with 10Hz frame rate. The positive sequences are real *calcium spikes* cropped from the training video aligned to the peak of the spike, whereas the negative sequences are randomly selected time periods from the rest non-spike periods. Specifically, consider training data $\mathcal{D} = \{\mathbf{D}_1, \dots, \mathbf{D}_N\}$, where $\mathbf{D}_n \triangleq (\mathbf{y}_n, l_n)$, with input sequence \mathbf{y}_n and output label $l_n \in \{0, 1\}$. Our goal is to learn model parameters θ to best characterize the mapping from \mathbf{y}_n to l_n with likelihood $p(\mathcal{D}|\theta) = \prod_{n=1}^N p(\mathbf{D}_n|\theta)$. In our setting for sequence classification, the input is a sequence, $\mathbf{y} = \{y_1, \dots, y_{T_0}\}$, where y_t is the input data at time t . There is a corresponding hidden state vector $\mathbf{h}_t \in \mathbb{R}^K$ at each time t , obtained by recursively applying the *transition function* $\mathbf{h}_t = g(\mathbf{h}_{t-1}, \mathbf{y}_t; \mathbf{W}, \mathbf{U})$. \mathbf{W} is *encoding weights*, and \mathbf{U} is *recurrent weights*. The output c for our classification is defined as the corresponding *decoding function* $p(c|\mathbf{h}_{T_0}; \mathbf{V}) = \sigma(\mathbf{V}\mathbf{h}_{T_0})$, where $\sigma(\cdot)$ denotes the *logistic sigmoid function*, and \mathbf{V} is *decoding weights*.

The transition function $g(\cdot)$ can be implemented with a *gated* activation function, such as LSTM [13] or a Gated Recurrent Unit (GRU) [21]. Both LSTM and GRU have been proposed to address the issue of learning long-term sequential dependencies. Each LSTM unit has a cell containing a state \mathbf{c}_t at time t . This cell can be viewed as a memory unit. Reading or writing the memory unit is controlled through sigmoid gates: input gate \mathbf{i}_t , forget gate \mathbf{f}_t , and output gate \mathbf{o}_t . The hidden units \mathbf{h}_t are updated as follows:

$$\begin{aligned} \mathbf{i}_t &= \sigma(\mathbf{W}_i \mathbf{y}_t + \mathbf{U}_i \mathbf{h}_{t-1} + \mathbf{b}_i), & \tilde{\mathbf{c}}_t &= \tanh(\mathbf{W}_c \mathbf{y}_t + \mathbf{U}_c \mathbf{h}_{t-1} + \mathbf{b}_c), \\ \mathbf{f}_t &= \sigma(\mathbf{W}_f \mathbf{y}_t + \mathbf{U}_f \mathbf{h}_{t-1} + \mathbf{b}_f), & \mathbf{c}_t &= \mathbf{f}_t \odot \mathbf{c}_{t-1} + \mathbf{i}_t \odot \tilde{\mathbf{c}}_t, \\ \mathbf{o}_t &= \sigma(\mathbf{W}_o \mathbf{y}_t + \mathbf{U}_o \mathbf{h}_{t-1} + \mathbf{b}_o), & \mathbf{h}_t &= \mathbf{o}_t \odot \tanh(\mathbf{c}_t), \end{aligned} \quad (1)$$

where \odot represents the element-wise matrix multiplication operator. Note that the training of RNNs is completed off-line, only the efficient testing stage is performed for seeds refinement.

In the testing stage, given an input $\tilde{\mathbf{y}}$ (with missing label \tilde{l}), the estimate for the output is $p(\tilde{l}|\tilde{\mathbf{y}}, \hat{\theta})$, where $\hat{\theta} = \arg \max \log p(\mathcal{D}|\theta)$. In our practical application, the testing sequence $\tilde{\mathbf{y}} \in \mathbb{R}^T$ is often of length $T > T_0$. We first convert it into a bag of subsequences $\{\tilde{\mathbf{y}}_i\}_{i=1}^{T-T_0+1}$, with a sliding window of width T_0 and moving step size 1. The well trained LSTMs are then used to label the subsequences. We consider $\tilde{\mathbf{y}}$ as positive if at least one subsequence in its bag is classified as "calcium spike" ($l = 1$), otherwise negative. Intuitively, this means that we only care about the patterns of neural spikes, regardless of their temporal positions. We will show the performance of the classifier in the Experiment section.

Seeds Merging Once the set of seeds is cleansed, there is still a low possibility of identifying multiple seeds within a single ROI. Therefore, we merge all these redundant seeds by computing the temporal similarity of seeds within their neighborhood, and preserving the one with maximum intensity. Specifically, we compute the similarity based on phase-locking information [22]. For a sequence, we extract the instantaneous phase dynamics using Hilbert transform, and only consider the subsequences containing prominent peaks, because all the pixels within the same ROI are highly correlated only during the calcium spiking periods, but not necessarily during baseline period. After seeds merging, we obtain K seeds, as the number of ROIs in our sc-CNMF.

Spatial and Temporal Initialization The time series of the k th seed is used as initial guess of temporal signal $\hat{\mathbf{s}}_k$. The spatial map of the corresponding ROI, $\hat{\mathbf{r}}_k$, is estimated by pooling neighbor pixels with temporal similarity above a threshold. Because of our seeds generating and cleansing approach, the spatiotemporal initialization in our method can be readily parallelized. Then we fine-tune the corresponding spatial and temporal guess, by applying semi-NMF: $\min \|\mathbf{z}_k - \hat{\mathbf{r}}_k \hat{\mathbf{s}}_k^\top\|$, where $\mathbf{z}_k \subset \mathbf{I}^s$ is a region containing the k th ROI. The spatial map is updated as $\mathbf{r}_k \leftarrow \mathbf{z}_k \mathbf{s}_k (\mathbf{s}_k^\top \mathbf{s}_k)^{-1}$, and the temporal signal is updated as $\mathbf{s}_k \leftarrow \mathbf{s}_k \sqrt{\frac{(\mathbf{r}_k \mathbf{z}_k)^+ + \mathbf{s}_k (\mathbf{r}_k^\top \mathbf{r}_k)^-}{(\mathbf{r}_k \mathbf{z}_k)^- + \mathbf{s}_k (\mathbf{r}_k^\top \mathbf{r}_k)^+}}$, where $\mathbf{M}^+ \triangleq \frac{|\mathbf{M}| + \mathbf{M}}{2}$ and $\mathbf{M}^- \triangleq \frac{|\mathbf{M}| - \mathbf{M}}{2}$ for any matrix \mathbf{M} [23]. In total, we now have K ROIs $\mathbf{S}^0 = [\mathbf{s}_1, \dots, \mathbf{s}_K]$, and temporal signals $\mathbf{R}^0 = [\mathbf{r}_1, \dots, \mathbf{r}_K]$. Similarly, the background parameters $\mathbf{b}^0, \mathbf{f}^0$ are also estimated by the same semi-NMF procedure, using $(\mathbf{I}^s - \sum_{k=1}^K \mathbf{r}_k \mathbf{s}_k^\top)$. $\mathbf{S}^0, \mathbf{R}^0, \mathbf{b}^0, \mathbf{f}^0$ are then used as initializations of CNMF.

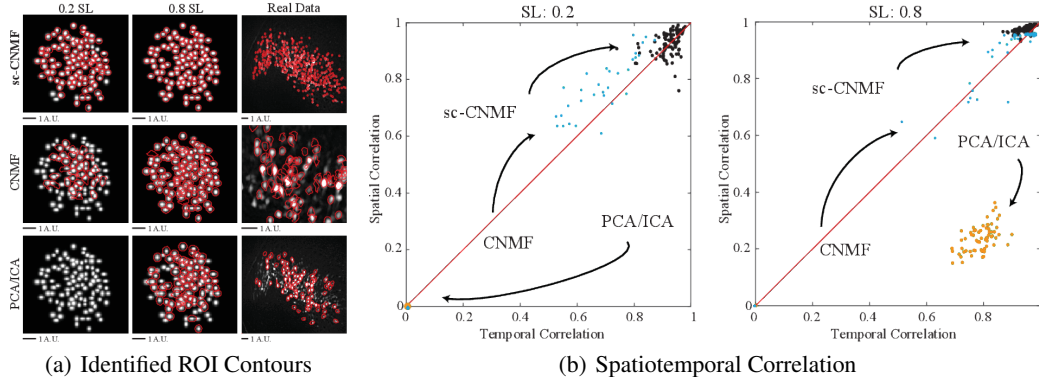


Figure 2: Visualization of the general performance. (a) A comparison of identified ROIs with contours between sc-CNMF, CNMF and PCA/ICA in simulated data of signal level (SL) 0.2 & 0.8 and real data. (b) Spatiotemporal correlation between the identified ROIs and ground truth by the three methods in simulated data of SL 0.2 & 0.8.

4 Experiments

We demonstrate the performance of sc-CNMF on both synthetic and real data. For simulation, we employ a scoring criterion that evaluates the performance, where we calculate the spatial and temporal similarity between the ground truth and the identified ROIs using rescaled cosine similarity. To measure the precision of the performance, we calculate true positive rate, false positive rate and false negative rate of the identified ROIs. This can reflect the level of spatial locality objectively. For real data, we use the contours to annotate the identified ROIs, and superimpose them to max projection of preprocessed videos to show the performance. The proposed methods are implemented in Matlab. We will release the codes once the paper is published. We also provide full resolution figures of visualization as well as an ablation study of each step in supplemental materials.

Simulation We synthesized 100 neurons with average neuron diameter γ_0 comparable to real data in a 128×128 field of view. Each neuron was simulated by a 2D Gaussian function with a variance in its two dimensions ($\gamma = \gamma_0 + \xi$, $\xi \sim \mathcal{N}(0, 1)$), and the calcium dynamics was generated by the first-order autoregressive process (decay time constant 0.95) with randomized spike events (spiking probability equals 1%), modified from [9]. The background was extracted from the real single-photon miniscope imaging videos [24], and temporal fluctuations of the background and spatial noises were added. The ground truth neural signals were then synthesized with the noisy background with a varying ratio, *signal level* (SL), ranging from 0.05 to 0.8 with a step size 0.05. Due to the biophysical property, the fluorescence is positively correlated to the light stimulation, thus the spatial positions of simulated neurons were densely generated in the high background illuminated area.

Real Data Miniscope calcium imaging data were collected from the barrel cortex of awake and freely behaving mice. The size of the raw videos were $1080 \times 1440 \times T_0$, with sampling rate 20Hz. For the performance test, we spatially downsampled the videos with a factor of 2 (540×720), and the temporal downsampling rate was 2. All experiments were conducted according to protocols approved by the Duke University Institutional Animal Care and Use Committee.

4.1 General Performance

We compare our methods with PCA/ICA and pure CNMF. PCA/ICA is the most popular semi-automatic method for processing miniscope calcium imaging [12]. We use the commercially available Mosaic software (Inscopix Inc.) [25] as PCA/ICA implementation, and process the data by following the standard work-flow in the software manual. In particular, we choose the number of principal components (PC) and independent components (IC) based on their suggested rate (*e.g.* 20% more ICs and 50% more PCs than the estimated number of ROIs). For CNMF, we use the default initialization strategy as described in [9].

In Fig. 2, we visualize the ROI detection results in (a) and their spatiotemporal correlation in (b). For both the real data and the simulations with signal levels at either 0.2 or 0.8, sc-CNMF can label

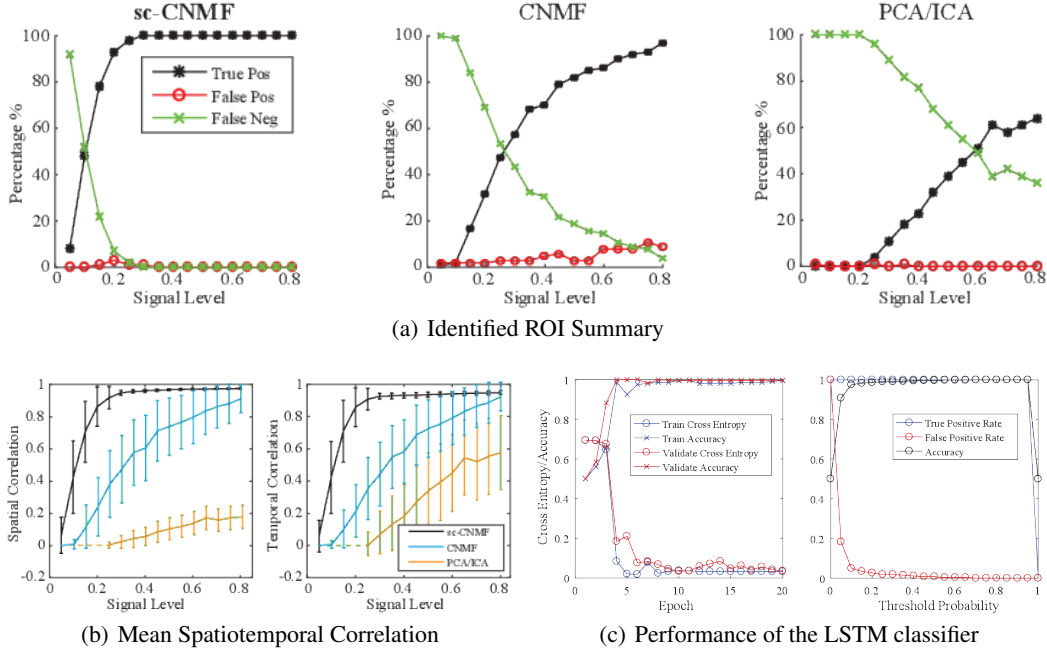


Figure 3: Quantification and comparison of the general performance. (a) A comparison of the average spatiotemporal correlation between the identified ROIs and the ground truth by the three methods. (b) Accuracy and precision of the three methods. (c) Performance of the LSTM classifier.

a nearly complete set of ROIs, whereas the other methods only label a small subset of ROIs, and perform poorly in extracting correct ROIs. The spatial and temporal correlation between ground truth and identified ROIs are significantly higher with the use of sc-CNMF than with the PCA/ICA method.

We show the performance comparisons for the full range of signal level in Fig. 3. The overall general performance of all methods decreases, as signal level diminishes. However, the proposed sc-CNMF remains highly effective within a reasonably wide signal range, and significantly outperform PCA/ICA across all SLs. Compared to the pure CNMF, sc-CNMF performs evidently superior at low and intermediate SLs, and more stably with optimal results at high SLs. Notice that the constantly low spatial correlation of PCA/ICA is due to its lack of spatial localization of identified ROIs.

4.2 Performance of Each Module

Neural Enhancing We examine the effectiveness of the neural enhancing module, in terms of eliminating the microscope-specific background effect. This is validated by comparing the performance of PCA/ICA method with and without neural enhancing module. For simulated data, we run the experiment on signal level 0.2 to 0.8 with a step of every 0.2, with the same PC and IC rate (here PC = 150 and IC = 120). The results are shown in Fig. 4. We find that our neural enhancing module significantly improves the performance of PCA/ICA. The number of identified ROIs and overall spatiotemporal correlation significantly increase at all SLs. Similarly, in the case of real data, the number of identified ROI increases compared to using raw data. There are still potential false positive and duplicated ROIs, but this can only be possibly overcome by manual intervention, which is due to the limitations of PCA/ICA method itself.

Seeds Cleansing We examine the importance of the seeds cleansing module in accurately selecting the valid set of ROI seeds. This is implemented by replacing the initialization module in the pure CNMF with our seeds cleansing module. The results are shown in Fig. 5. In the default initialization of CNMF, we chose $K = 120$ to provide the tolerance of false positives. Despite this, there exist several neurons not detected. Because K is greater than the ground truth, we see that the pure CNMF can (1) miss true ROIs, (2) generate duplicate seeds within a single ROI, and (3) include false positives when signal-to-noise ratio is not high enough. In the initialization of our sc-CNMF,

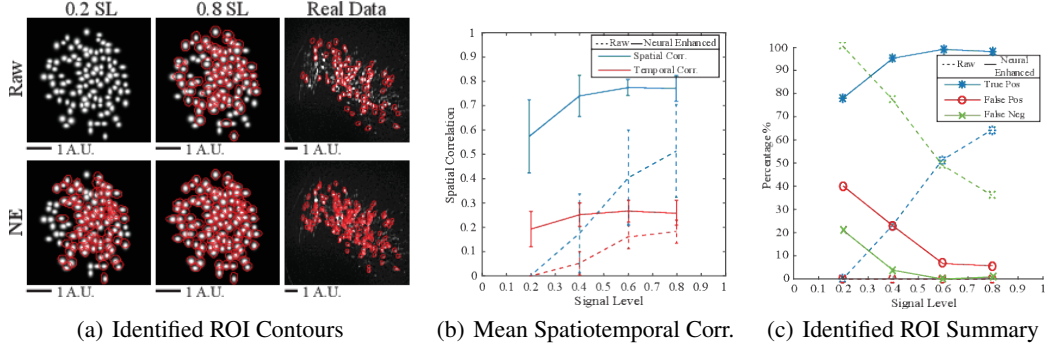


Figure 4: Improvements of using the neural enhanced (NE) video in PCA/ICA. (a) Visualization of the identified ROIs with contours using the raw or the NE video as an input to PCA/ICA. (b) A comparison of the average spatiotemporal correlation between the identified ROIs and the ground truth using the raw or the NE video. (c) Accuracy and precision of the two inputs.

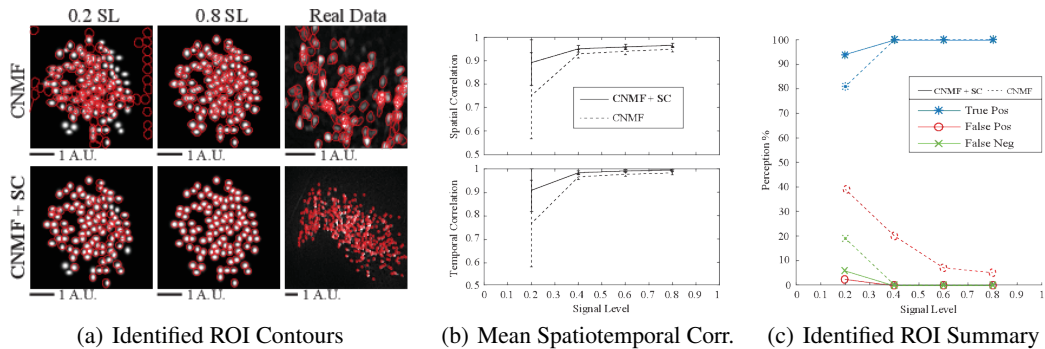


Figure 5: Improvements of the seeds cleansing (SC) in CNMF. (a) Visualization of the identified ROIs using the pure CNMF or the SC. (b) A comparison of the average spatiotemporal correlation between the identified ROIs and the ground truth with the pure CNMF or the SC. (c) Accuracy and precision of the two processes.

a maximally correct set of ROIs is returned, without tuning the number of ROIs by trial-and-error. The last but not the least note is that for real data, CNMF cannot successfully finish computation of the full size dataset, due to memory overflow with the same hardware setting, thus we can only crop the video to compute a small patch. sc-CNMF, on the other hand, does not have this problem. We provide a demo video as a supplement, showing the raw, neural enhanced and fully processed results by sc-CNMF from real data (<https://goo.gl/XnTw3C>).

5 Conclusions

In this work, we develop the neural enhancing and seeds cleansing modules to provide high quality initialization to the modified CNMF framework. These two novel modules, integrated with the modified CNMF framework, allow us to accurately extract neural signals from miniscope calcium imaging. For neural enhancing, we employ frame-wise morphological opening to approximate the dynamic background in imaging videos, and to smooth the signals by anisotropic diffusion. For seeds cleansing, we used GMM as a coarse seeds classifier, and a custom RNN/LSTM to detect a tight set of valid seeds. Notice that the seeds cleansing module is the first method to integrate deep learning in the field of neural signal extraction of single-photon based calcium imaging. We post-process the set of seeds by merging and “same-ROI suppressing” to form an accurate final set of ROI seeds. We then integrated the modified CNMF framework for refining spatial maps and temporal signals of detected ROIs. The experimental results on both synthetic and real data confirm that sc-CNMF outperforms the PCA/ICA and pure CNMF methods, and is the first seed-accurate framework in extracting spatiotemporal calcium signals from miniscope based single-photon imaging.

References

- [1] S. Peron, J. Freeman, V. Iyer, C. Guo, and K. Svoboda. A cellular resolution map of barrel cortex activity during tactile behavior. *Neuron*, 86(3), 2015.
- [2] J. Stirman, I. Smith, M. Kudenov, and S. Smith. Wide field-of-view, multi-region, two-photon imaging of neuronal activity in the mammalian brain. *Nature Biotechnology*, 2016.
- [3] B. Flusberg, A. Nimmerjahn, E. Cocker, E. Mukamel, R. Barretto, T. Ko, L. Burns, J. Jung, and M. Schnitzer. High-speed, miniaturized fluorescence microscopy in freely moving mice. *Nature methods*, 5(11), 2008.
- [4] K. Ghosh, L. Burns, E. Cocker, A. Nimmerjahn, Y. Ziv, A. El Gamal, and M. Schnitzer. Miniaturized integration of a fluorescence microscope. *Nature methods*, 8(10), 2011.
- [5] E. Mukamel, A. Nimmerjahn, and M. Schnitzer. Automated analysis of cellular signals from large-scale calcium imaging data. *Neuron*, 63(6), 2009.
- [6] J. Reidl, J. Starke, D. Omer, A. Grinvald, and H. Spors. Independent component analysis of high-resolution imaging data identifies distinct functional domains. *Neuroimage*, 34(1), 2007.
- [7] M. Pachitariu, A. Packer, N. Pettit, H. Dalgleish, M. Hausser, and M. Sahani. Extracting regions of interest from biological images with convolutional sparse block coding. In *Advances in NIPS*, 2013.
- [8] R. Maruyama, K. Maeda, H. Moroda, I. Kato, M. Inoue, H. Miyakawa, and T. Aonishi. Detecting cells using non-negative matrix factorization on calcium imaging data. *Neural Networks*, 55, 2014.
- [9] E. Pnevmatikakis, D. Soudry, Y. Gao, T. Machado, J. Merel, D. Pfau, T. Reardon, Y. Mu, C. Lacefield, W. Yang, et al. Simultaneous denoising, deconvolution, and demixing of calcium imaging data. *Neuron*, 89(2), 2016.
- [10] N. Aporthe, A. Riordan, R. Aguilar, J. Homann, Y. Gu, D. Tank, and S. Seung. Automatic neuron detection in calcium imaging data using convolutional networks. In *Advances In Neural Information Processing Systems*, 2016.
- [11] D. Cai, D. Aharoni, T. Shuman, J. Shobe, J. Biane, W. Song, B. Wei, M. Veshkini, M. La-Vu, J. Lou, et al. A shared neural ensemble links distinct contextual memories encoded close in time. *Nature*, 534(7605), 2016.
- [12] S. Resendez, J. Jennings, R. Ung, V. Nambodiri, Z. Zhou, J. Otis, H. Nomura, J. McHenry, O. Kosyk, and G. Stuber. Visualization of cortical, subcortical and deep brain neural circuit dynamics during naturalistic mammalian behavior with head-mounted microscopes and chronically implanted lenses. *Nature protocols*, 11(3), 2016.
- [13] S. Hochreiter and J. Schmidhuber. Long short-term memory. In *Neural computation*, 1997.
- [14] P. Mitra and B. Pesaran. Analysis of dynamic brain imaging data. *Biophysical journal*, 76(2), 1999.
- [15] B. Efron, T. Hastie, I. Johnstone, and R. Tibshirani. Least angle regression. *The Annals of statistics*, 32(2), 2004.
- [16] R. Van Den Boomgaard and R. Van Balen. Methods for fast morphological image transforms using bitmapped binary images. *CVGIP: Graphical Models and Image Processing*, 54(3), 1992.
- [17] P. Perona and J. Malik. Scale-space and edge detection using anisotropic diffusion. *IEEE Transactions on pattern analysis and machine intelligence*, 12(7), 1990.
- [18] J. Vogelstein, B. Watson, A. Packer, R. Yuste, B. Jedynek, and L. Paninski. Spike inference from calcium imaging using sequential monte carlo methods. *Biophysical journal*, 97(2), 2009.
- [19] J. Vogelstein, A. Packer, T. Machado, T. Sippy, B. Babadi, R. Yuste, and L. Paninski. Fast nonnegative deconvolution for spike train inference from population calcium imaging. *Journal of neurophysiology*, 104(6), 2010.
- [20] Y. LeCun, Y. Bengio, and G. Hinton. Deep learning. *Nature*, 2015.
- [21] K. Cho, B. Van Merriënboer, C. Gulcehre, D. Bahdanau, F. Bougares, H. Schwenk, and Y. Bengio. Learning phrase representations using RNN encoder-decoder for statistical machine translation. In *EMNLP*, 2014.
- [22] T. Hahn, B. Sakmann, and M. Mehta. Phase-locking of hippocampal interneurons' membrane potential to neocortical up-down states. *Nature neuroscience*, 9(11), 2006.
- [23] C. Ding, T. Li, and M. Jordan. Convex and semi-nonnegative matrix factorizations. *IEEE transactions on pattern analysis and machine intelligence*, 32(1), 2010.
- [24] P. Zhou, S. Resendez, G. Stuber, R. Kass, and L. Paninski. Efficient and accurate extraction of in vivo calcium signals from microendoscopic video data. *arXiv preprint arXiv:1605.07266*, 2016.
- [25] J. Jennings, R. Ung, S. Resendez, A. Stamatakis, J. Taylor, J. Huang, K. Veleta, P. Kantak, M. Aita, K. Shilling-Scriver, et al. Visualizing hypothalamic network dynamics for appetitive and consummatory behaviors. *Cell*, 160(3), 2015.

Supplementary Material of Seeds Cleansing CNMF

A Additional Results

A.1 Full Scale Visualizations of the Imaging Data

For better visualization of the identified ROI contours, we provide the larger-scale figures. The overall performance of the proposed sc-CNMF is in Fig. S1, the improvement by neural enhancement module is in Fig. S2, and the improvement by seeds cleansing module in Fig. S3.

For further investigation of the effectiveness of each module, we did the ablation study on each module, and visualize the results as the max projection in Fig. S4 & Fig. S5, and the detected seeds in Fig. S6.

A.2 Notes on the Supplemental Video

The *Raw* video shows the raw imaging data, while the *Preprocessed* and the *Processed* video represents the video after neural enhancing and the full sc-CNMF separately. Specifically, after neural enhancing we can get the preprocessed video with every frame enhanced, but no separated spatiotemporal information of individual ROIs. However, after the whole process we do get every ROI and its corresponding temporal signal separated. We then take the product of the separated spatial and temporal matrix to retrieve the video version as the processed video. We also include the video in the supplemental materials.

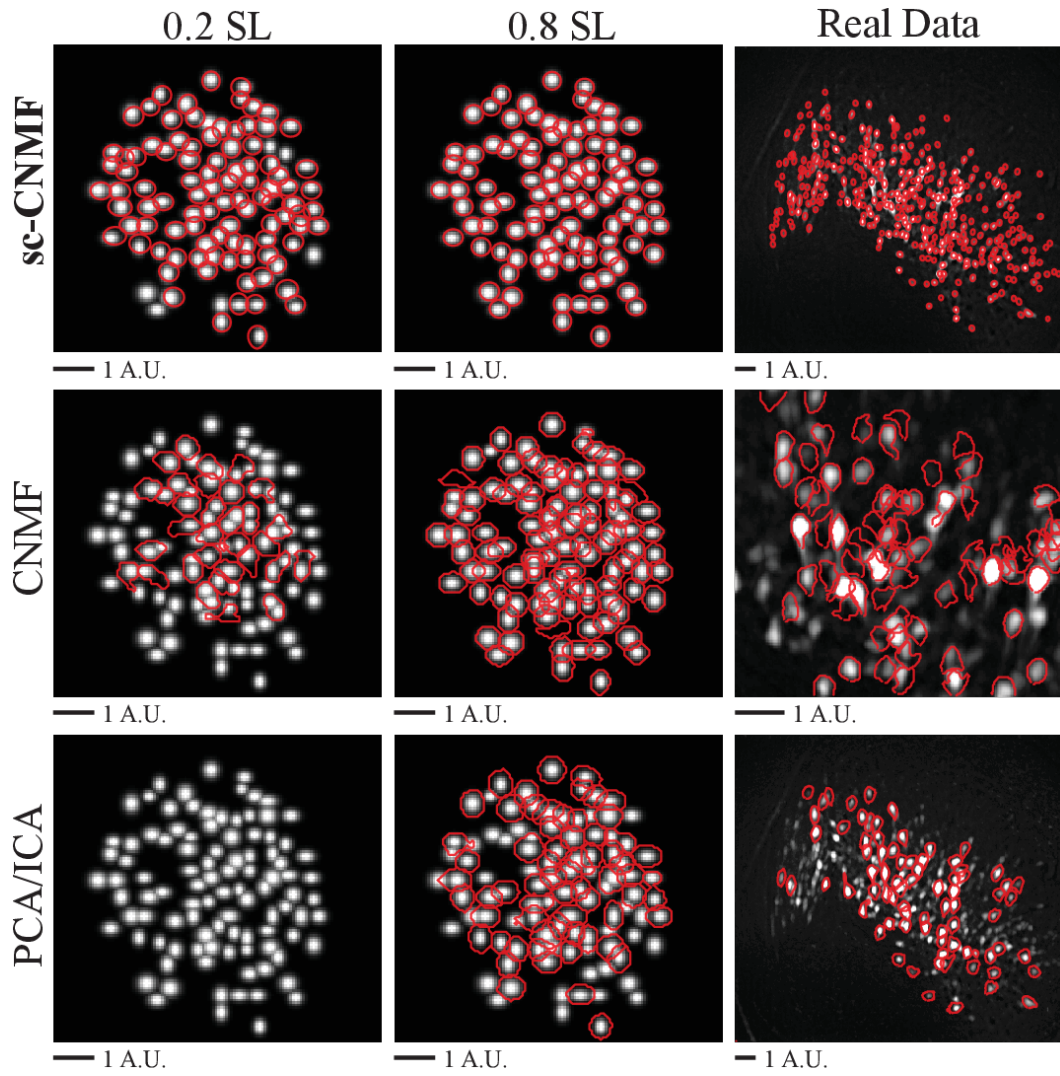


Figure S1: Visualizations of the identified ROI contours of the three methods on simulated datasets (SL 0.2 & 0.8) and real data.

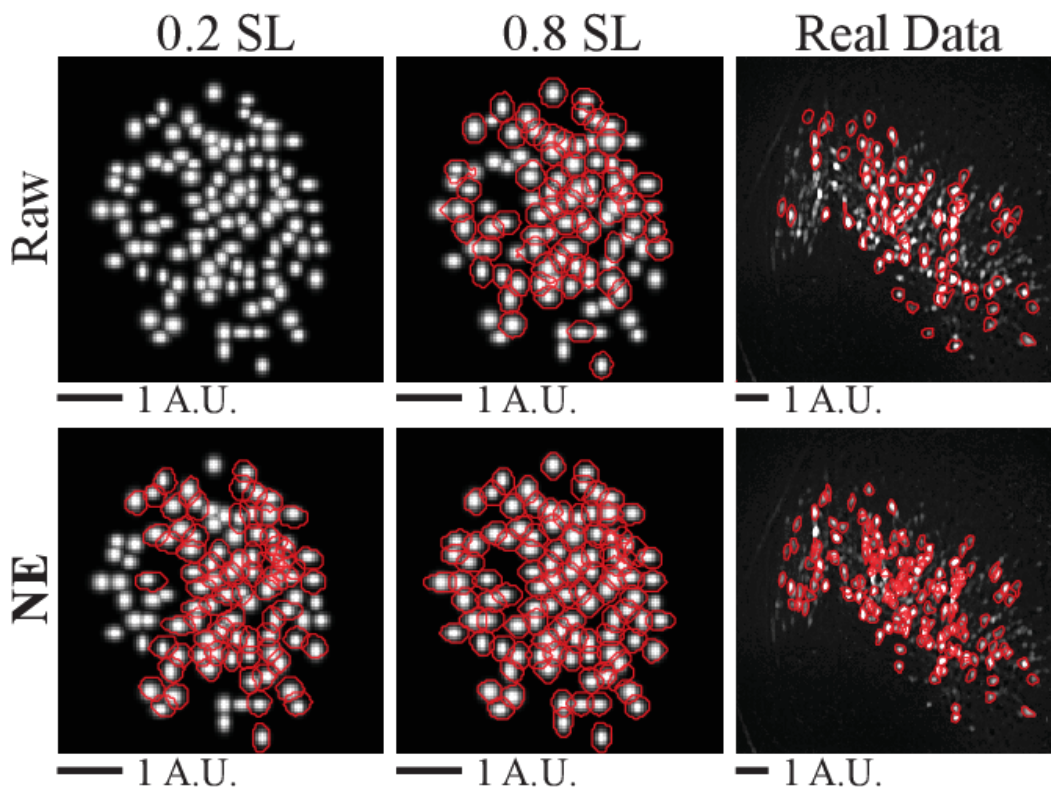


Figure S2: Visualizations of the identified ROI contours using raw data or NE data as input, in the cases of simulated datasets (SL 0.2 & 0.8) and real data.

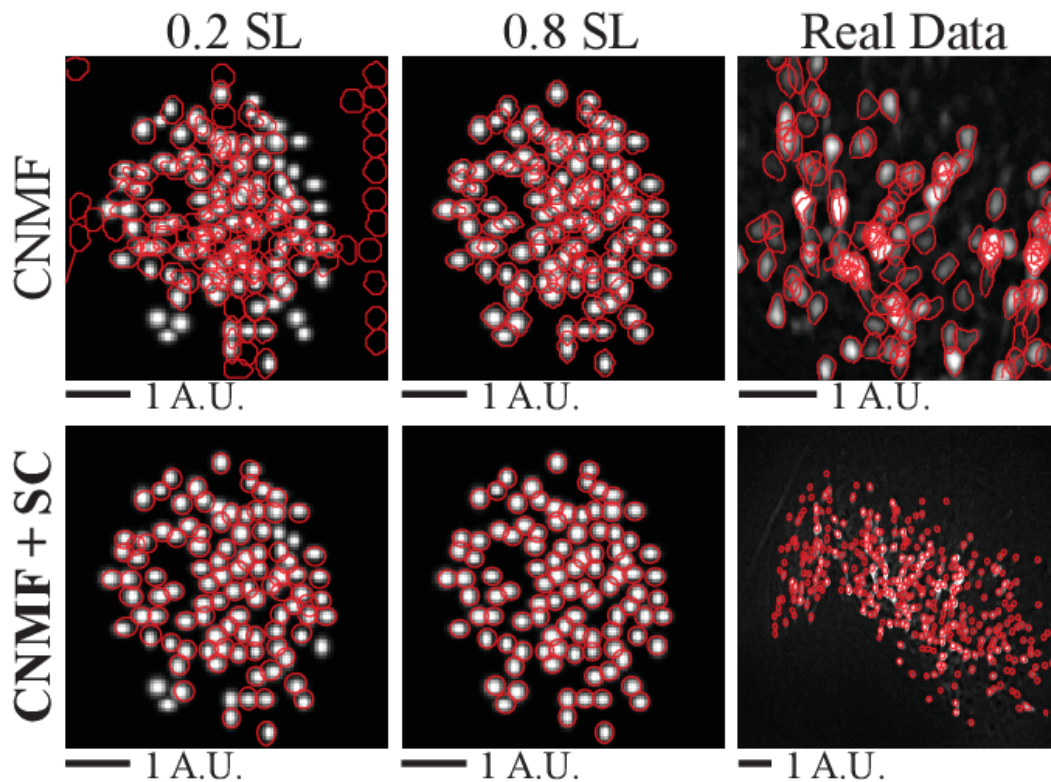


Figure S3: Visualizations of the identified ROI contours using the pure CNMF or the seeds cleansing module, in the cases of simulated datasets (SL 0.2 & 0.8) and real data.

A.3 Detailed Visualization of the Effect at Each Step

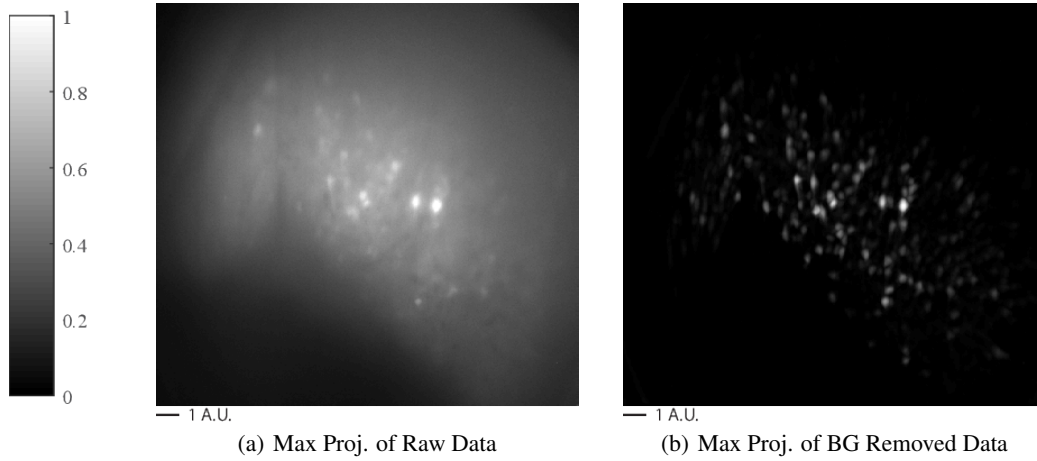


Figure S4: Visualizing the effect of background (BG) removal. (a) Max projection of the raw data, which contains significantly more BG noise as well as unbalanced and dominating BG illumination, compared to (b) the max projection of the BG removed version, which optimally removes BG illumination and maximally suppresses noises.

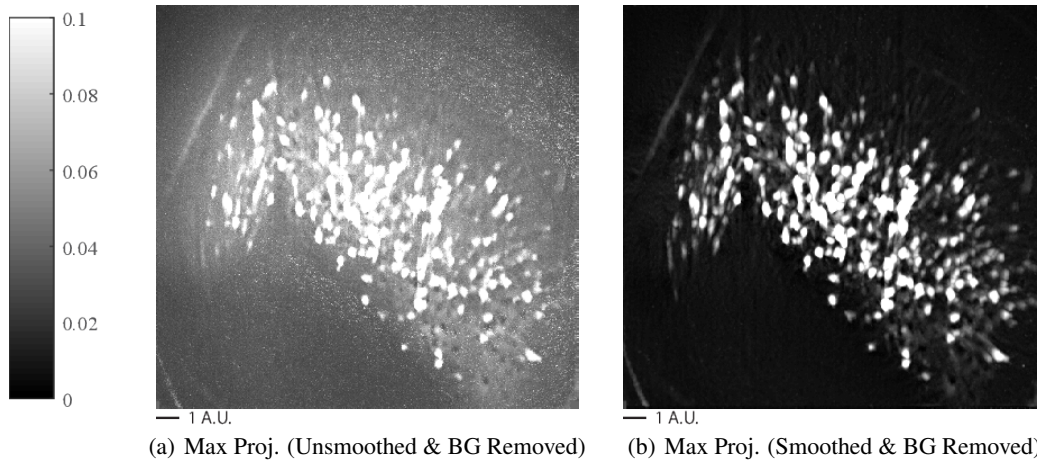
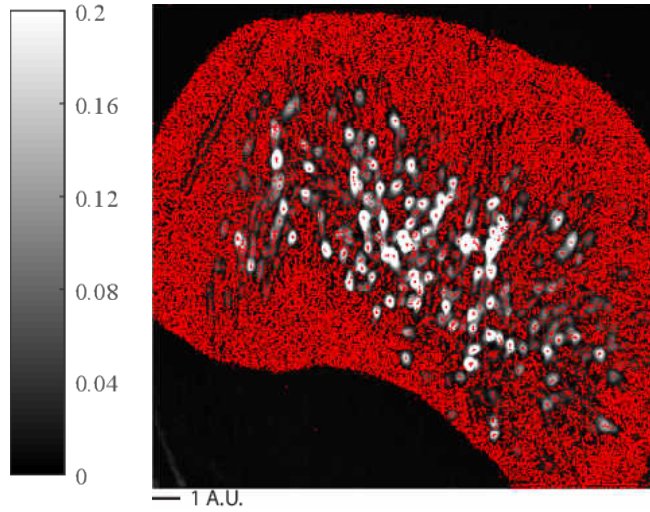
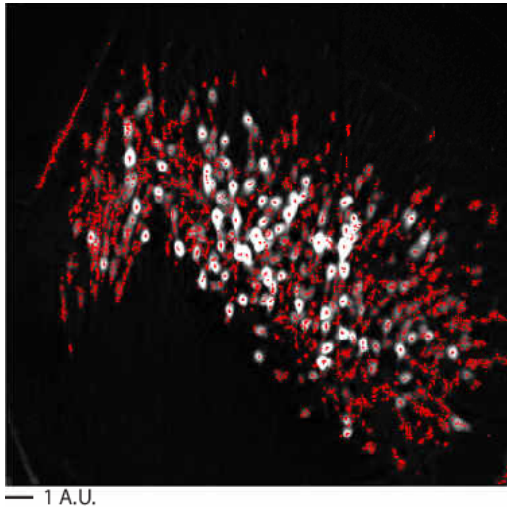


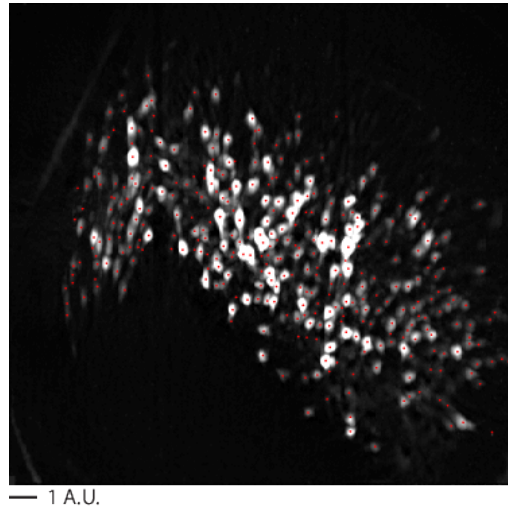
Figure S5: Visualizing the effect of smoothing. (a) Max projection of the background (BG) removed data after smoothing, which results in a much higher signal-to-noise Ratio, compared to (b) the max projection of the unsmoothed version. The intensity range of all the pixel is normalized to $[0, 1]$



(a) Over-complete Seeds



(b) Seeds Cleansed after GMM



(c) Seeds Cleansed after LSTM

Figure S6: Visualizing the effect of GMM & LSTM. (a) Over-complete set of seeds found as local maxima. (b) Seeds cleansed using GMM. False positives are significantly removed while true positives are remained. (c) Seeds cleansed using LSTM. False positives are maximally eliminated while only one seed per ROI is remained.